OPEN ACCESS
IOP Publishing
Journal of Physics B: Atomic, Molecular and Optical Physics
J. Phys. B: At. Mol. Opt. Phys. **58** (2025) 245001 (14pp)
https://doi.org/10.1088/1361-6455/ae270e

Wavelength-dependent photodissociation of MgH^+ via intermediate resonances

Dilfuza Umarova, Otabek Umarov and András Csehi*

Department of Theoretical Physics, Faculty of Science and Technology, University of Debrecen, PO Box 400, H-4002, Debrecen, Hungary

E-mail: csehi.andras@science.unideb.hu

Received 4 July 2025, revised 14 November 2025
Accepted for publication 30 November 2025
Published 12 December 2025

Abstract

We study by means of theoretical and numerical methods the resonance-enhanced two-photon dissociation of the MgH^+ molecule, driven by narrow-band Gaussian laser pulses of various parameter values. Fine tuning the photon wavelength in the energy region of an intermediate electronic state ($\lambda \sim 200$–310 nm), we reveal rich nuclear dynamics, including Rabi oscillations and dynamic interference. Upon solving the time-dependent Schrödinger equation of the nuclei, the fingerprints of these dynamical effects are identified in the energy spectrum of the emitted molecular fragments. We also show that the dipole coupling between the intermediate resonances and the vibrational continuum varies very sensitively with the photon wavelength, allowing for an efficient control of the depletion, and of the bound-state dynamics of the molecule.

Keywords: photodissociation, Rabi oscillation, dynamic interference, resonance-enhancement, dipole coupling, quantum coherent control

1. Introduction

Steering and tracing the time evolution of atomic scale systems with short laser pulses are key elements of coherent quantum control [1–7]. Several different control techniques have been developed over the past decades to drive atomic and molecular species from a given initial state to a final desired quantum state, with high efficiency [8–15]. Among them, are of particular interest, when the complete time-dependent quantum trajectory is controlled according to user-defined pathways for the state populations and phases [16, 17]. In this respect, minimal level descriptions with simple analytic solutions were found to be very useful, as they can provide a transparent interpretation of complex physical phenomena [18]. Wavelength control of dissociation [19–22] and ionization phenomena [23, 24] has been widely applied to enhance dissociation and ionization yields, by hitting intermediate resonant states during multiphoton transitions. As the dynamic Stark shifts (DSSs) of the involved atomic or molecular levels adiabatically follow the intensity envelope of the applied high-frequency laser pulse [25, 26], the conditions for resonance-enhancements are substantially modified in strong radiation fields.

Under intense radiation fields, the populations of the (near-)resonantly coupled quantum states periodically oscillate. These Rabi oscillations (ROs) [27, 28] are characteristic to non-linear coherent quantum dynamics, when the system can be well approximated as being two-level. Owing to the resonant or near-resonant coupling with the laser pulse, two decaying dressed states are formed with time-dependent

* Author to whom any correspondence should be addressed.

energies, that follow the envelope function of the laser pulse in opposite directions. At the rising edge of the pulse the energy splitting of the dressed states increases, and becomes maximal at the center of the pulse (Rabi splitting). Then on the falling edge, the splitting decreases back to zero. Absorption of additional photon(s) can lead to the break-up of the coherently driven system, as a result of which the Autler–Townes (AT) doublet appears in the spectrum of the emitted particles. Particles emitted from the higher (lower) dressed state are predominantly responsible for the higher (lower) energy side of the AT doublet. ROs of atomic electrons have been widely investigated over the last four decades [29–43]. Recently, they have gained renewed interest, which was mainly caused by the availability of strong, ultrafast XUV pulses. The resonantly driven atom undergoing damped ROs, is ionized with a certain probability at each Rabi cycle. The temporal interference of electrons emitted with different time delays gives rise to pronounced multipeak pattern of the AT doublet. Other characteristics of the doublet, such as the splitting, shifting or asymmetry also carry important information about the underlying dynamics of the bound electrons. In particular, the asymmetry of the AT doublet was attributed to different factors, including for example the photon energy detuning [36], the DSSs of the participating levels [31, 32], the energy-dependence of the bound-to-continuum dipoles [34], the loss of the intermediate level [18], the interference of resonant and nonresonant ionization pathways [35–37], the shape of the pulse envelope [32, 40], or the phase of the driving field [29, 30].

The multipeak pattern of the photoelectron spectrum in strong laser pulses can be also formed by dynamic interference (DI), as it was demonstrated in direct one-photon ionization [44–46]. Whenever the two conditions are simultaneously fulfilled [45]: 1) the peak relative DSS of the initial and final states is larger than the pulse bandwidth; 2) the depletion of the initial state is small, DI can become operational leading to pronounced intensity modulations of the spectrum. Here, the underlying physical phenomenon is the temporal interference of electrons that are emitted with the same kinetic energy, but with a certain time delay, at the rising and falling edges of the laser pulse. In the last years, the DI have been studied from different perspectives [47–54], including its recent experimental observation by applying an attosecond pulse train combined with a pair of IR lasers [55].

For below-threshold photon energies, when the break-up process can happen via resonance-enhancements, similar conditions to observe DI have been put forward [56]. Detuning the photon frequency from the exact resonance was found key in satisfying these conditions simultaneously. For non-zero detuning, the Rabi splitting of the dressed states can well exceed the pulse bandwidth, meanwhile the ionization of the atom is naturally kept small, due to the reduced efficiency of transition in the off-resonant laser. Since the ROs are washed out for off-resonant driving, the multi-peak pattern of the AT doublet is mainly dictated by the DI [57].

In this paper, we study the resonance-enhanced two-photon dissociation of the MgH^+ ion [58–61], at various photon

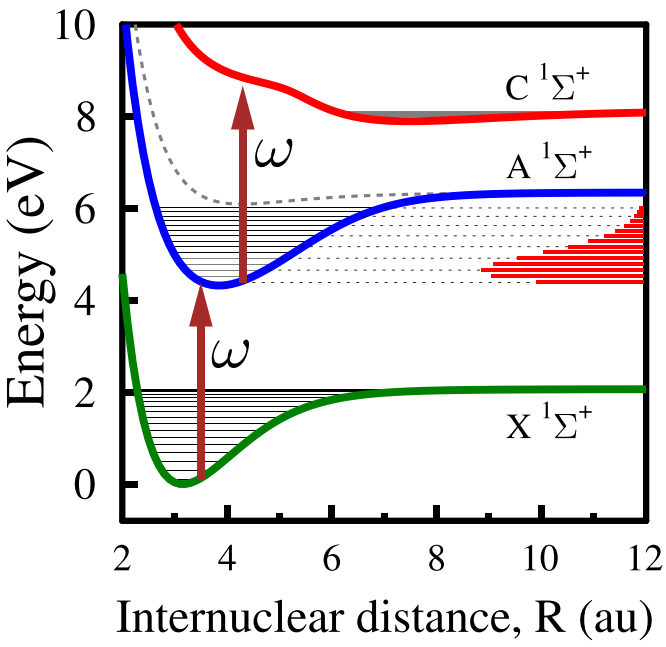

Figure 1. Ground- and low-lying potential energy curves of the MgH^+ molecule, relevant for the $(1+1)$ photon resonance-mediated dissociation studied in this paper. Depending on the photon frequency ω, intricate nuclear dynamics are generated between the X and A electronic states, which are probed by the dissociating molecular fragments in the C electronic state. The red horizontal bars indicate the strength of the dipole coupling from the $X(\nu = 0)$ ground vibrational level to $A(\nu_A)$.

wavelengths. As the intermediate A state of MgH^+ lies energetically halfway between the X an C states in the Franck–Condon region, this molecule is perfectly suitable for studying $1+1$ photon resonance-enhanced multiphoton dissociation phenomena (see figure 1). Fine tuning the photon energy in the region of the intermediate bound electronic state of the molecule, we reveal intricate nuclear dynamics, the fingerprints of which are identified in the energy spectrum of the emitted fragments. In agreement with previous results reported in resonance-enhanced multiphoton ionization (REMPI), we find that when the dissociation happens at exact resonance, the ROs of the nuclei dominate the spectrum. On the other hand, when the laser is detuned from the exact resonance, the DI of molecular fragment amplitudes governs the spectrum shape. Furthermore, we show that the dissociation yield is very efficiently controlled, owing to the sensitive energy-dependence of the dipole coupling strength from the intermediate resonances to the continuum.

2. Results

To reveal the role of the A electronic state in the photodissociation dynamics of MgH^+, in this section, we will apply different photon energies in the region of $\omega \sim 4$–6 eV (or alternatively $\lambda \sim 200$–310 nm). The vibrating molecule, that interacts with the laser pulse given in equations (3) and (4), is

assumed initially (at $t=-\infty$) in its absolute ground state $X(\nu=0)$. We set the pulse duration parameter sufficiently long ($T=500$ fs) to make the pulse bandwidth narrow enough, $\delta\omega=4\sqrt{\ln 2}/T\approx 4.4\times10^{-3}$ eV. Such narrow spectral width of the laser pulse is necessary for a quasi-selective vibronic excitation of the molecule, as the energy spacing between the neighboring vibrational levels of the X and A states is of the order of a few tenths of eV. This small value of $\delta\omega$ thus in general allows for a transparent interpretation of the system dynamics. However, as will be clear below, even a minor population of the other levels can strongly influence the dissociation dynamics under certain conditions.

In what follows, we simulate the dissociation dynamics accurately, by solving the TDSE with equation (5). Utilizing weak laser pulses of $I_0=10^8\,\mathrm{W\,cm^{-2}}$ peak intensity ensures that the molecule does not complete more than half a Rabi cycle at the resonant wavelengths, namely smooth transitions are induced between $X(\nu=0)$ and $A(\nu_A)$. As seen in figure 2(a), the dissociation probability in the C state, obtained after expiration of the laser pulse, varies very abruptly with the photon energy. Even though the dipole coupling values from $X(\nu=0)$ to $A(\nu_A)$, seen in figure 2(c), exhibit a regular behavior reminiscent of the Franck–Condon factors, neither the transition probability to A (see figure 2(b)), nor the corresponding dissociation probability in figure 2(a) reflect this behavior. The reason behind is attributed to the very different dipole coupling strength from the $A(\nu_A)$ vibrational levels to the C manifold. These dipole couplings are shown in figure 3 for $\nu_A=0,1,2,3$. Here, the dipole curves—shown by the solid red lines—exhibit pronounced oscillatory shapes directly reflecting the shapes of the corresponding vibrational eigenstate wave functions of the molecule. The number of peaks follows ν_A+1, while the number of nodes is equal to ν_A. For completeness, the dissociation probabilities generated by weak pulses when the molecule is initialized in the respective eigenstate $A(\nu_A)$, are also shown in figure 3 by the broken lines. These dissociation probabilities nicely reflect the energy-dependence of the dipole values shown by the solid lines.

Figure 3 helps elucidating the irregular behavior found in figure 2(a) and in figure 2(b) for the dissociation- and excitation probabilities, respectively. For example, at the photon energy that is resonant with the $X(\nu=0)\rightarrow A(\nu_A=0)$ transition ($\omega\approx4.2868$ eV), a nonnegligible amount of population is transferred to the A state ($p_A\approx0.09$), but the dissociation probability remains extreme low (see figure 2(a) at $\nu_A=0$). This is due to the very low dipole value from $A(\nu_A=0)$ to the continuum of the C state, as indicated by the vertical solid line in figure 3(a). Contrary, when the laser resonantly excites the molecule from the $X(\nu=0)$ to the $A(\nu_A=1)$ state ($\omega\approx4.422$ eV), dissociation becomes very efficient due to the strong dipole coupling from $A(\nu_A=1)$ to the C manifold (see the vertical solid line in figure 3(b)). In the case of the $A(\nu_A=2)$ state, this dipole has an intermediate value (figure 3(c)), while for $A(\nu_A=3)$ it becomes moderate again (figure 3(d)), which are reflected in the corresponding dissociation probabilities in figure 2(a).

Concluding figures 2 and 3, very different bound-state dynamics and dissociation probabilities are expected, depending on which intermediate vibrational level is hit resonantly during the interaction with the laser. Moreover, the sensitive energy-dependence of the bound-to-continuum dipoles demonstrated above is expected to strongly affect the dynamics also for off-resonant driving. In such a case, a selective population transfer cannot be realized and the populations of the vibrational levels become more balanced. Below, we discuss separately the resonant and off-resonant dissociation of MgH^+.

2.1. Resonant dissociation

In this subsection, we consider the dissociation of MgH^+ following exact resonant transitions, namely when $\omega=\omega_{A(\nu_A)}-\omega_{X(\nu=0)}$. To induce nontrivial vibronic dynamics, the pulse duration parameter is unchanged $T=500$ fs, but the peak laser intensity is increased to $I_0=10^{11}\,\mathrm{W\,cm^{-2}}$. For these values of the laser parameters, the molecule executes several Rabi oscillations between the X and A states, as demonstrated in the middle columns of figure 4 for $\nu_A=0,1,2,3,4,5$. Here, the number of completed Rabi cycles can be roughly estimated from the actual value of the pulse area $\eta=\int_{-\infty}^{\infty}\varepsilon_0\mu g(t)\mathrm{d}t=\varepsilon_0\mu\sqrt{\pi}T$, where μ is the corresponding dipole moment between the $X(\nu=0)$ and $A(\nu_A)$ states. These pulse area values are indicated at the right side of figure 4. Clearly, when the ν_A-C dipole coupling, and hence the dissociation yield is small, complete Rabi oscillations are generated with high contrast (see figure 4(b)), and the value of η nicely correlates with the number of completed Rabi cycles. However, when the ν_A-C dipole is strong, and hence dissociation happens with high probability, the Rabi oscillations are substantially damped, preventing the correlation between η and the number of Rabi cycles. For example, in the extreme case when $X(\nu=0)$ and $A(\nu_A=1)$ are coupled resonantly, a complete dissociation happens during the rising edge of the laser pulse. As seen in figure 4(e), approximately two Rabi floppings are generated (the third one has very low amplitude) instead of the seven, that was predicted by the pulse area.

From the higher vibrational levels ($\nu_A>1$), the MgH^+ molecule also dissociates very efficiently. This is demonstrated by the large depletion of the bound populations (middle panels of figure 4), in accordance with the high dissociation yields in the right panels of figure 4. Here, the ramp-ups in the population- and dissociation curves indicate that dissociation occurs in a step-wise manner. Whenever some vibrational level $A(\nu_A)$ is maximally populated, dissociation becomes possible upon absorption of a second photon that promotes the molecule to the repulsive C state. This gives rise to the ramp-ups in the C populations (dashed lines in the right panels of figure 4), while the flat parts correspond to the time moments when the molecule is returned to the ground level $X(\nu=0)$ and

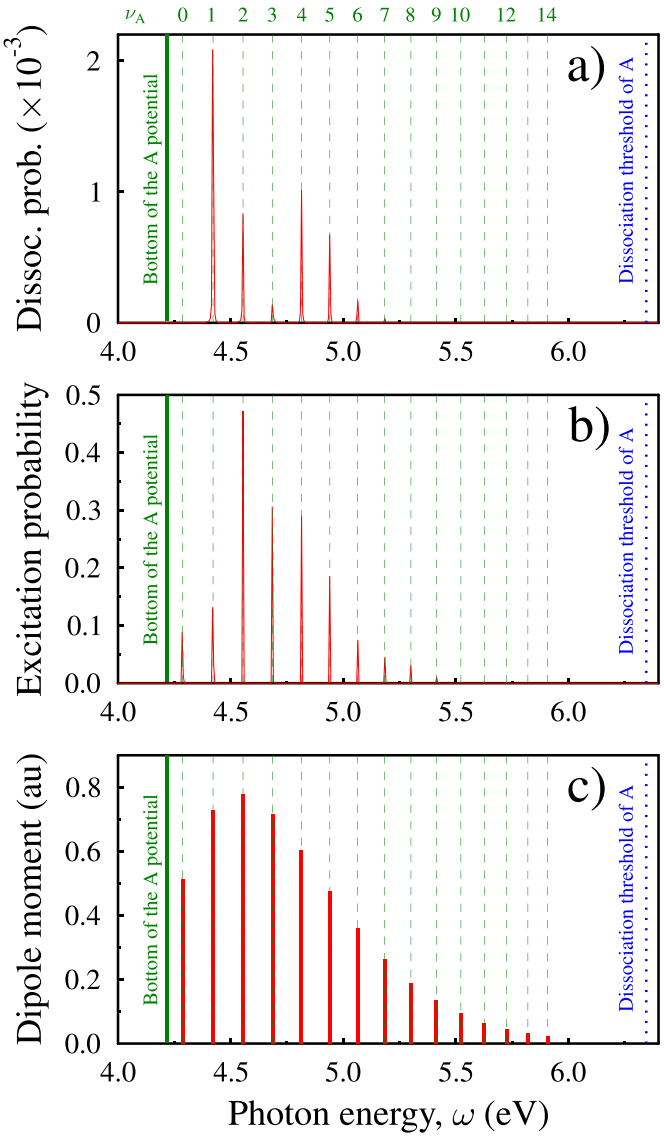

Figure 2. Photon energy-dependent dissociation of MgH^+ via intermediate vibrational levels of the A electronic state. (a) Final dissociation probabilities in the C electronic state, generated by weak laser pulses of $I_0 = 10^8\,\mathrm{W\,cm^{-2}}$ peak intensity and $T = 500\,\mathrm{fs}$ duration (for these parameter values, the molecule does not complete more than half a Rabi cycle between $X(\nu = 0)$ and $A(\nu_A)$). (b) Corresponding final excitation probabilities of the A electronic state. These transition probabilities do not follow the strength of the dipole couplings between $X(\nu = 0)$ and $A(\nu_A)$, shown in (c), because of the very different dipole coupling strengths from $A(\nu_A)$ to the C manifold (see text and figure 3). The vertical dashed lines indicate the energy positions of some vibrational levels of the A electronic state.

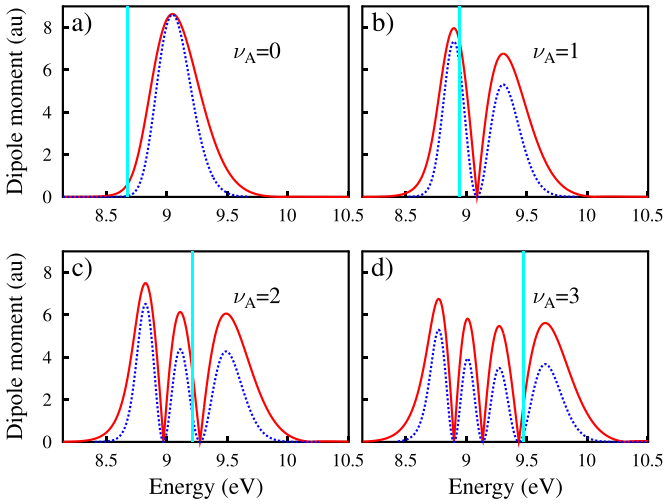

Figure 3. Absolute values of the dipole couplings between the $\nu_A = 0, 1, 2, 3$ vibrational states of the A electronic state and the C manifold (solid curves). The broken curves show the scaled ($\times 250$) dissociation probabilities generated by weak laser pulses of $I_0 = 10^8\,\mathrm{W\,cm^{-2}}$ peak intensity and $T = 500\,\mathrm{fs}$ duration, when the molecule is initialized in its respective vibrational state in the A electronic state. These dissociation probabilities follow the oscillatory shape of the dipole curves and directly reflect the shape of the given vibrational state wave function. The vertical solid lines represent the nominal spectrum positions (the expected centers of the spectra in the weak-field limit) for exact resonant transitions: $\omega_{\varepsilon_0} = \omega_{X(\nu=0)} + 2 \times \omega_{\mathrm{res}}$, where $\omega_{\mathrm{res}} = \omega_{A(\nu_A)} - \omega_{X(\nu=0)}$ is the actual resonant photon energy.

thus dissociation is closed. The dissociation curves in figure 4 are time-delayed with respect to the population curves of C. These time delays directly reflect how long it takes for the molecular wave packet to reach the complex absorbing potential (CAP) region, placed at $R_c = 30\,\mathrm{au}$, where it is completely absorbed.

The energy spectra of emitted molecular fragments after resonance-enhancements are shown in the left panels of figure 4. Several spectral features can be observed, such as splitting, shifting, multipeak pattern or asymmetry, which have been widely investigated in atomic ionization processes. Importantly, the AT spectra of MgH^+ presented here exhibit very similar behavior as those found previously for photoelectrons. As it has been shown earlier for electrons, the multipeak spectral pattern is directly linked to the Rabi floppings completed during the break-up process [57]. We recently demonstrated this correspondence also for molecular dissociation, with the help of a simple analytic model [62]. It was shown that the multipeak pattern of the spectrum is attributed to the temporal interference of fragment amplitudes that were emitted at the distinct Rabi cycles. As a result, which is also evident from figure 4, when the molecule completes N Rabi floppings, N ramp-ups are seen in the dissociation curves, and the corresponding spectrum features N peaks. Some of these peaks have low yield, and some of them are not fully developed. We note here that utilizing narrower pulse bandwith could allow for a better resolution of the subpeaks of the AT doublets. Furthermore, the impact of neighboring levels could be also minimized for such pulses.

To be specific, now we continue with a deeper analysis of the $\nu_A = 2$ case (third row of panels in figure 4). When the $X(\nu = 0)$ state is coupled resonantly with $A(\nu_A = 2)$, the molecule executes approximately 7.5 Rabi floppings, in accordance with the pulse area value $\eta = 7.65 \times (2\pi)$. Owing to the notable dipole strength with the C manifold, seen in figure 3(c), the amplitudes of these Rabi oscillations rapidly decrease over time (figure 4(h)). As a result, a dissociation probability of more than 80% is realized by the end of the

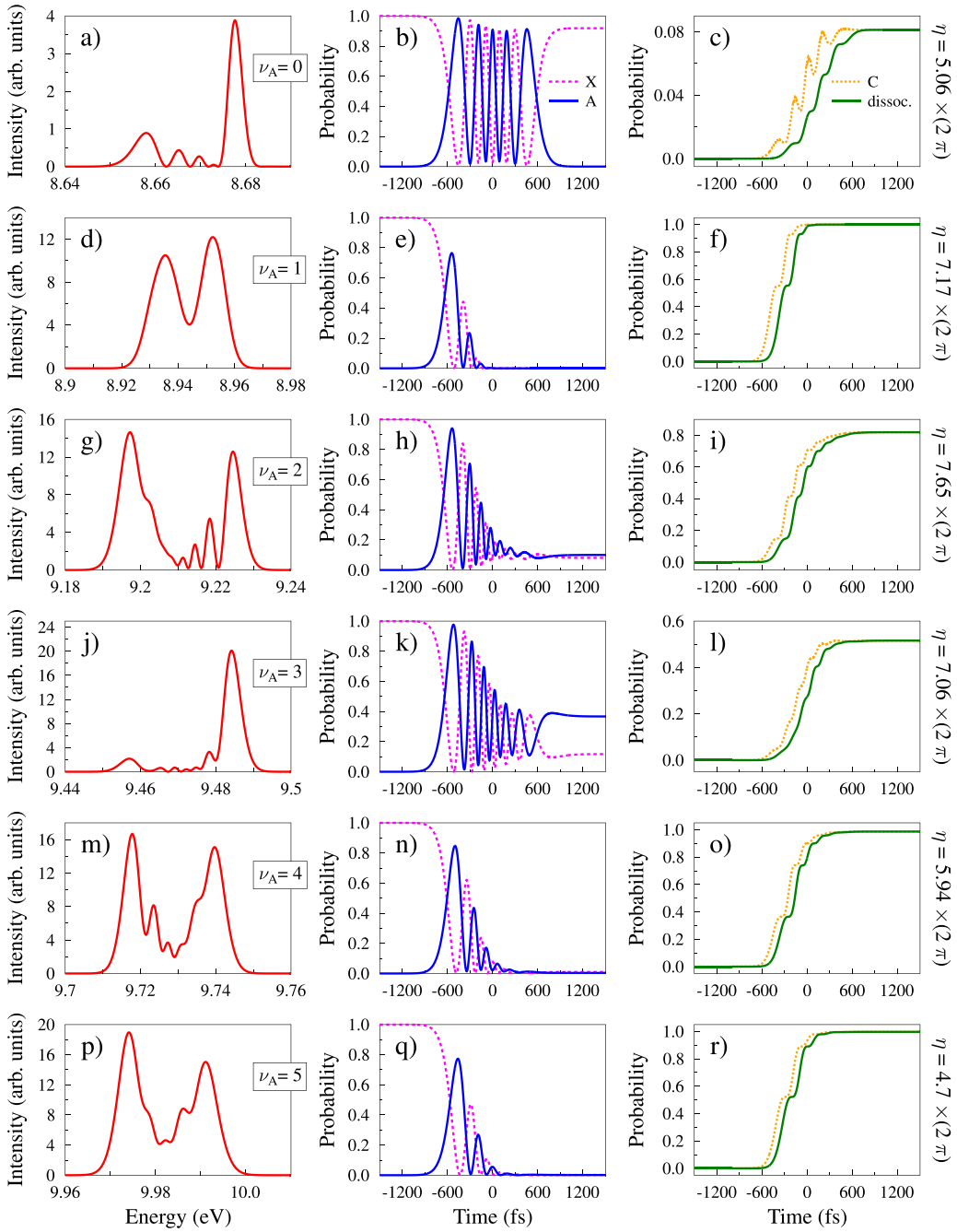

Figure 4. Resonance-enhanced $(1+1)$ photon dissociation of MgH^+ at photon energies that are exactly resonant for the $X(\nu=0) \rightarrow A(\nu_A)$ vibronic transitions ($\nu_A = 0, 1, 2, 3, 4, 5$). $I_0 = 10^{11}\,\mathrm{W\,cm^{-2}}$ peak laser intensity and $T = 500$ fs pulse duration are applied to generate several Rabi oscillations between the resonantly coupled vibronic states. (left panels) Fragment energy spectra exhibiting pronounced multipeak patterns, that are directly related to the Rabi oscillatory bound-state dynamics of the molecule (see text for details). (middle panels) Time-dependent electronic state populations, featuring several Rabi oscillations between the X and A states. The number of Rabi oscillations depends on the respective bound–bound dipole coupling, and is further modified by the bound-continuum coupling that induces depletion. (right panels) Time-dependent populations (broken lines) and dissociation probabilities (solid lines) in the C state. The actual values of the η pulse area are shown on the right side. The presented results were obtained upon solving the TDSE of the vibrating molecule accurately.

interaction. According to figure 5(b), the population of the $A(\nu_A = 2)$ vibronic state is more than two orders of magnitude larger than those of the other levels of the A state. This would imply that the final spectrum shape is exclusively determined by the $A(\nu_A = 2)$ state. To unravel the possible role of the other neighboring states in the formation of the spectrum, we calculate the fragment energy distribution with the multi-level model, by gradually including more and more states of A in the description. As seen in figure 5(c), when only the $A(\nu_A = 2)$ is included, most of the spectral features are recovered, but the correct symmetry cannot be captured. However, when the adjacent $A(\nu_A = 1)$ and $A(\nu_A = 3)$ states are added (dark blue line), all the spectral features—including the correct asymmetry—are recovered. Inclusion of

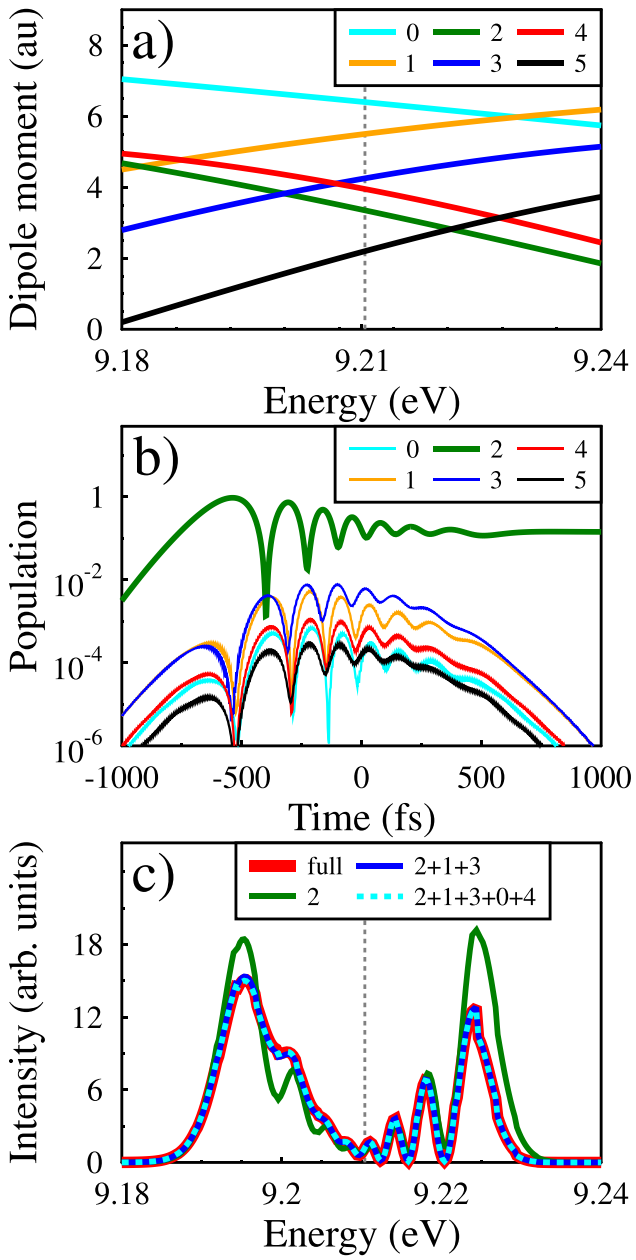

Figure 5. Resonance-enhanced $(1+1)$ photon dissociation of MgH^+ via the $\nu_A = 2$ intermediate level. The applied photon energy is resonant with the $X(\nu = 0) \rightarrow A(\nu_A = 2)$ transition ($\omega = 4.5551$ eV) and the remaining laser parameter values are $I_0 = 1 \times 10^{11}\,\mathrm{W\,cm^{-2}}$, $T = 500$ fs. (a) Absolute values of the dipole couplings between the $A(\nu_A = 0,1,2,3,4,5)$ states and the C manifold, shown in the energy region of the spectrum. (b) Time-dependent populations of the $A(\nu_A = 0,1,2,3,4,5)$ vibrational states. (c) Energy spectra calculated with the multi-level method upon gradually including more and more vibrational levels of the A electronic state. The vertical dashed lines indicate the nominal positions of the spectra ($\omega_{\varepsilon_0} = \omega_{X(\nu=0)} + 2\omega$).

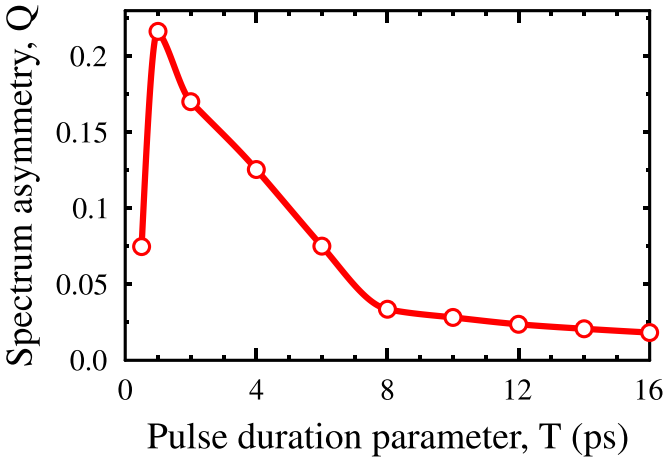

Figure 6. Spectrum asymmetry parameter Q (equation (1)), computed for different pulse durations, keeping the pulse area constant $\eta = 7.65 \times (2\pi)$. The applied photon energy is resonant with the $X(\nu = 0) \rightarrow A(\nu_A = 2)$ transition ($\omega = 4.5551$ eV). The first data point corresponds to the spectrum shown in figure 4(g).

further states does not modify the spectrum shape significantly (light blue dashed line). It is thus evident from figure 5(c), that the nearby $A(\nu_A = 1)$ and $A(\nu_A = 3)$ states modify the overall symmetry of the spectrum. Furthermore, these two vibronic states become responsible for the merging of the spectral peaks around ~9.2 eV in figure 5(c). Despite their low population, the role of these states in the dissociation dynamics becomes relevant due to their strong dipole with the C continuum, as demonstrated in figure 5(a). Although, the $A(\nu_A = 0)$ and $A(\nu_A = 4)$ states also have notable dipoles, the suppressed population of these distant states does not allow them to substantially participate in the formation of the spectrum. Considering the $\nu_A = 1,2,3$ states is thus sufficient to get convergent spectrum with the multi-level method (thick red line in figure 5(c)), which nicely agrees with the accurate spectrum obtained from wave packet propagation (figure 4(g)).

Let us now inspect the asymmetry of the spectrum obtained after dissociation via the $A(\nu_A = 2)$ state. As has been reported in studies on resonant ionization, in general, the spectrum asymmetry is caused by several factors, including for example the Stark shifts of the involved levels, the energy-dependence of the bound-to-continuum dipoles, the participation of other states, or the interplay between different break-up pathways. Consequently, exactly symmetric spectra are encountered very rarely, under special circumstances. To quantify the asymmetry of the spectrum, and hence, to identify when it happens to be symmetric, we introduce the asymmetry parameter

$$Q = \frac{|Q_\mathrm{L} - Q_\mathrm{H}|}{Q_\mathrm{L} + Q_\mathrm{H}}, \tag{1}$$

with Q_L and Q_H being the heights of the lower- and higher energy prominent peaks of the AT doublet, respectively. Values of $Q \approx 1$ imply a strong asymmetry of the spectrum, while $Q = 0$ indicates a completely symmetric spectrum. As seen in figure 6, the impact of the different factors that give rise to the spectrum asymmetry can be minimized with long pulses, meanwhile keeping the pulse area constant. Upon transition from $T = 500$ fs to $T = 1000$ fs, all the spectral peaks are fully resolved in the lower energy half of the spectrum (around ~ 9.2 eV), and as a result the lower prominent peak of the AT

doublet is greatly enhanced. This still increases the asymmetry, but beyond $T = 1000$ fs the spectrum monotonically approaches the symmetric shape. Owing to the narrow spectral width and the small intensity of the long pulses in figure 6, the Stark shifts and the role of other states are gradually eliminated. For $T > 8$ ps, the decreasing of Q slows down, which is attributed to the very steep energy-dependence of the $A(\nu_A = 2) - C$ dipole function in the vicinity of the nominal spectrum position (see figure 3(c)). For other states, achieving $Q = 0$ could be realized with shorter pulses.

2.2. *Off-resonant dissociation*

In what follows, we discuss the more general scenario, when the laser photon energy is not resonant with any of the intermediate vibrational levels of A. In the case of off-resonant driving, the pronounced Rabi oscillations found in section 2.1 are completely washed out. This is demonstrated in figure 7, where the photon energy is set $\omega = 4.18$ eV, which is below the bottom of the A potential energy curve. To compensate the reduced efficiency of population transfer, here the peak laser intensity is increased to $I_0 = 5.3 \times 10^{11}\,\mathrm{W\,cm^{-2}}$. As is clear from figure 7(b), the amount of transferred population decreases with the vibrational state label ν_A. However, in contrast to the resonant case in figure 5, here the population distribution among the different $A(\nu_A)$ vibronic levels is more balanced, with no single highly dominant state, like in figure 5(b). As a consequence, in the off-resonant case, the dipole coupling of the different $A(\nu_A)$ states with the C continuum gains higher significance in the spectrum formation. This is demonstrated in figure 7(c), where the spectrum is calculated with the multi-level model, by gradually including more and more levels of A. Interestingly, all the spectral features are recovered already with the $\nu_A = 0$ state, except the correct dissociation yield. To capture the correct spectrum height, vibronic states up to $\nu_A \approx 10$ have to be included in the multi-level model. Despite their low population, the notable dipole moments of these states with the C state (see figure 7(a)) render them inevitable in the description, to get convergent results.

Adding states with $\nu_A \leqslant 4$ in the multi-level model, the spectrum height gradually increases (see the blue line in figure 7(c)), which is mainly caused by the increasing dipole strength of these states. On the other hand, the contribution of the $\nu_A > 4$ levels lead to decreasing spectrum intensity, until the accurate spectrum shape—shown by the thick red line in figure 7(c) - is finally recovered. The different contribution of the lower- and higher vibronic states to the spectrum shape is attributed to the constructive and destructive interference of the fragment amplitudes that are released from the distinct $A(\nu_A)$ states. Regarding the asymmetry of the spectrum, we note that in the case of off-resonant driving the AT doublet cannot be made symmetric with long pulses, like in the resonant case in figure 6. Due to the notable detuning of the laser from the exact resonance, the converged spectrum in figure 7(c) features strong asymmetry, which is in line with previous findings reported on atomic ionization spectra [36, 57]. In the

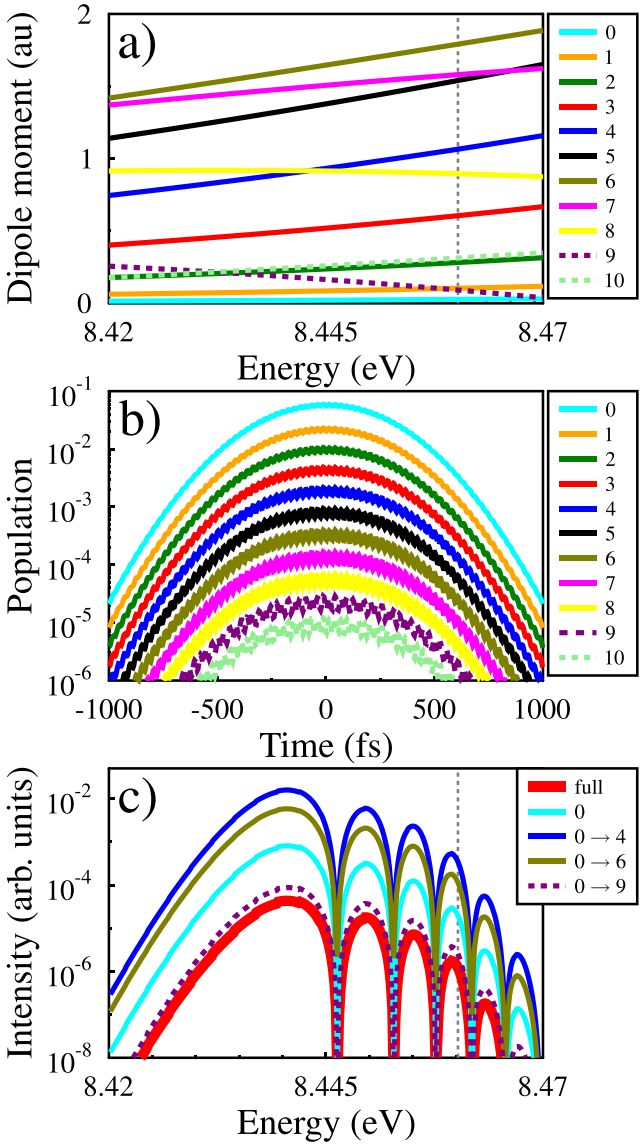

Figure 7. Two-photon dissociation of MgH^+ driven off-resonantly, via several intermediate levels $A(\nu_A)$. The applied photon energy is set below the bottom of the A potential curve ($\omega = 4.18$ eV) and the remaining laser parameter values are $I_0 = 5.3 \times 10^{11}\,\mathrm{W\,cm^{-2}}$, $T = 500$ fs. (a) Absolute values of the dipole couplings between the $A(\nu_A = 0, 1, \ldots 10)$ states and the C manifold, shown in the energy region of the spectrum. (b) Time-dependent populations of the $A(\nu_A = 0, 1, \ldots 10)$ vibrational states. (c) Energy spectra calculated with the multi-level method upon gradually including more and more vibrational levels of the A electronic state. The vertical dashed lines indicate the nominal positions of the spectra ($\omega_{\varepsilon_0} = \omega_{X(\nu=0)} + 2\omega$).

specific case of red (or negative) detuning applied here, the lower energy peak of the AT doublet near 8.44 eV in figure 7(c) is significantly enhanced with respect to the higher energy peak (not shown in figure 7). Upon approaching the exact resonance with the photon energy, the large value of the asymmetry parameter $Q \approx 1$ in figure 7(c), is greatly suppressed to small values—similar to those in figure 6—characteristic to

near-resonant AT doublets. Furthermore, we mention here that when the photon energy is set in between two vibronic levels, Rabi oscillations are still washed out, and the dissociation dynamics is very similar to that shown in figure 7. Fine tuning the photon wavelength between two vibronic levels, makes the populations of those two states the highest, and the depletion of the molecule will be stronger, since the $\nu_A - C$ dipoles are in general much larger for > 8.5 eV than for < 8.5 eV (see figure 3).

Finally, it is an intriguing question what is the cause of the multipeak spectral intensity modulations found in figure 7(c). Since Rabi oscillations are completely washed out in off-resonant driving, the underlying physical mechanism must be something else. The multipeak spectral pattern in figure 7(c), bears resemblance with that reported recently in REMPI under off-resonant pulses, in [56, 57]. There, the oscillatory pattern of the AT doublet was attributed to the DI of photoelectrons, ionized with the same energy at the rising and falling edges of the pulse. The two essential conditions to observe DI could be simultaneously fulfilled by off-resonant driving: 1) the Rabi splitting of the dressed states $W = \sqrt{\Omega^2 + \Delta^2}$, where $\Omega = \varepsilon_0 \mu$ is the Rabi frequency and $\Delta = \omega - \omega_{\rm res}$ is the detuning from the resonance, could well exceed the pulse bandwidth; 2) meanwhile the depletion of the atom could be naturally kept small due to the reduced efficiency of transition to the intermediate state. Here, the physics is similar except that the participants are nuclei instead of electrons. To see the possible role of DI in the multipeak pattern of the spectrum, we follow [57] and apply asymmetric laser pulses in the next subsection.

2.3. Asymmetric pulses

In this subsection, we consider asymmetric Gaussian envelope functions, given by the following expression

$$g(t) = \begin{cases} e^{-t^2/T_1^2} & \text{if } t \leqslant 0 \\ e^{-t^2/T_2^2} & \text{if } t > 0. \end{cases} \qquad (2)$$

Here, T_1 and T_2 are the pulse duration parameters on the rising and falling edges of the pulse, respectively. To keep the pulse area constant, the restriction $T_1 + T_2 = 2T$ is imposed, where T is the pulse duration parameter of the symmetric pulse in equation (4). The constant pulse area allows one to study pulse shape effects, including for example the role of DI in the break-up process. Upon transition from a perfectly symmetric envelope function ($T_1 = T_2 = T$) to a completely asymmetric one with $T_1 = 2T$ and $T_2 = 0$, the pulse suddenly drops to zero after its maximum. This reduces the possible role of DI in the dissociation.

As seen in figure 8(a), in the case of resonant dissociation, the number of spectral peaks is unaffected by the symmetry of the envelope function. Owing to the constant value of the pulse area, the number of completed Rabi cycles remains the same for symmetric and asymmetric pulses. The fact that the multipeak pattern of the spectrum is hardly affected by the completely asymmetric envelope, reveals that the shape of the AT doublet is primarily governed by Rabi oscillations, and DI only plays a minor role in resonant dissociation.

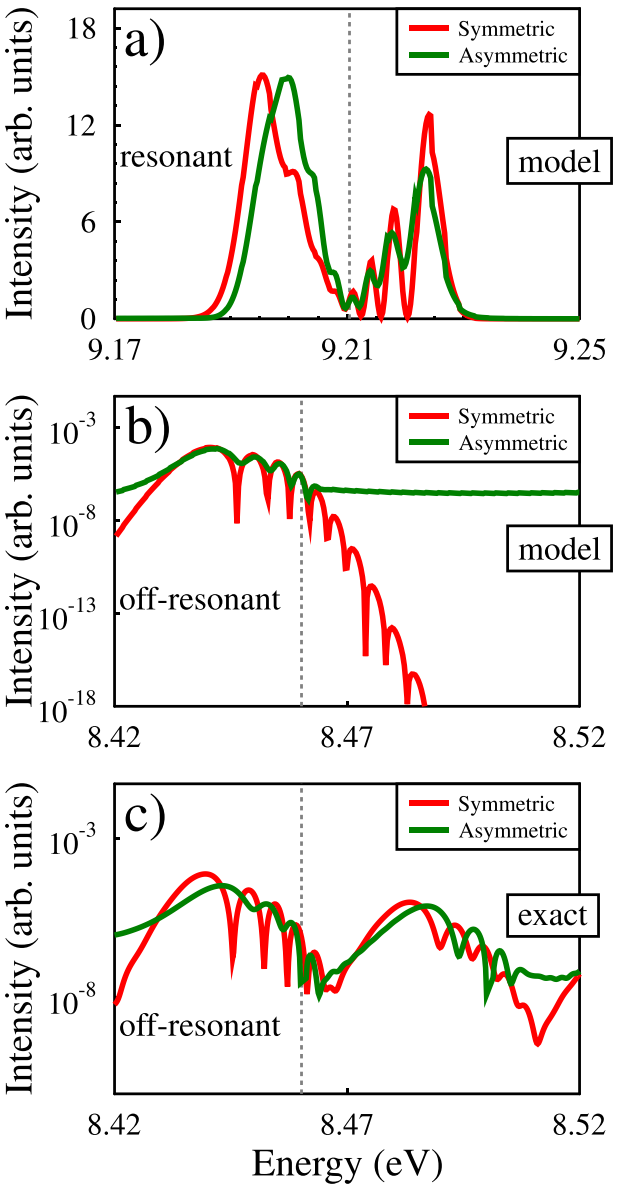

Figure 8. Energy spectra of MgH^+ obtained with symmetric ($T = 500$ fs) and asymmetric ($T_1 = 1000$ fs; $T_2 = 0$) pulses, following (a) resonant and (b)–(c) off-resonant driving. The applied I_0, T and ω values in (a) and (b)–(c) are identical to those in figures 5 and 7, respectively. For resonant driving in (a), the number of spectral peaks is unaffected by the symmetry of the pulse. Contrary, for off-resonant driving, the multipeak spectral pattern and the depletion are strongly modified by the asymmetric pulse, as given by the model in (b). This effect is washed out by the electric permanent dipole of the C state, as given by the exact solution in (c). The vertical dashed lines indicate the nominal positions of the spectra ($\omega_{\varepsilon_0} = \omega_{X(\nu=0)} + 2\omega$).

On the contrary, when the dissociation is driven off-resonantly, the multipeak pattern of the spectrum is substantially modified by the asymmetric envelope (see figure 8(b)). This indicates the important role of DI in the spectrum shape obtained with the symmetric pulse. As both conditions to

observe DI are fulfilled in the off-resonant, symmetric laser pulse, DI can become operational giving rise to intensity modulations of the spectrum. Under the asymmetric envelope in figure 8(b), the fragment emission on the falling edge is reduced. As a result, the spectral intensity modulations found for the symmetric envelope are mostly washed out. The low-contrast peaks that remain visible at $\omega_\varepsilon < \omega_{\varepsilon_0}$, are attributed to the interference of fragment amplitudes that were emitted shortly before the maximum of the asymmetric envelope. Since it is the interference of the same momenta from two time-delayed wave packets (see also [63] for atomic ionization), which gives rise to the modulation in the spectrum, there is still dynamic interference possible even, and especially with the half pulse which certainly contains the fragment momenta also present in the first wave packet.

The spectra in figure 8(a) provided by the multi-level model, are perfectly supported by the exact solution of the TDSE (not shown here). However, the model spectra in figure 8(b) obtained for off-resonant laser pulses, do not agree with the exact solution for $\omega_\varepsilon > \omega_{\varepsilon_0}$, as demonstrated in figure 8(c). Here, the permanent dipole of the C electronic state, which is included in the full solution but excluded from the model, makes the identification of DI more difficult. Thus, we envision that the demonstration of DI will be easier in apolar molecules, that have no electric permanent dipole moment.

Finally, we would like to demonstrate another great advantage of asymmetric envelope functions. As we could see in figure 7(b), the molecule executes a single Rabi cycle in the off-resonant laser pulse. The populations of the different $A(\nu_A)$ vibronic states increase during the rising edge of the pulse, then decrease on the falling edge. The dynamics of the C state population also follows this behavior (not shown here). This is because the fragment amplitudes promoted to the C state on the rising edge, get deexcited to the bound states on the falling edge. As a result, only a minor population remains in the C state by the end of the interaction, that can dissociate. We mention here that the large temporary population of the C state manifests in a large peak in the time-resolved spectrum around ~ 9.1 eV, that disappears by the end of the symmetric pulse. The application of asymmetric laser pulses with $T_1 > T_2$ can minimize the recapture from the continuum on the falling edge, leading to increased dissociation probabilities. This is demonstrated in figure 9, for two different peak laser intensities. Clearly, when $T_1 > 900$ fs, and hence $T_2 < 100$ fs, the dissociation yield is efficiently controlled through approximately three orders of magnitude. For a completely asymmetric pulse ($T_1 = 1000$ fs, $T_2 = 0$), p_{diss} can be significantly increased by reducing fragment recapture on the falling edge of the pulse.

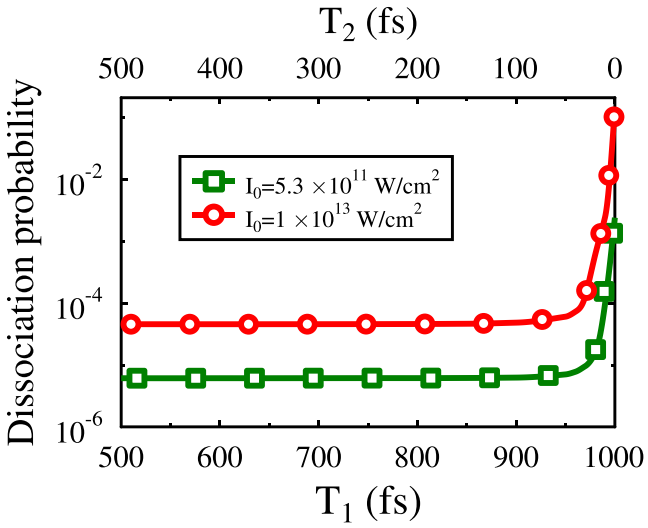

Figure 9. Dissociation probabilities of off-resonantly driven MgH^+, obtained with different asymmetric envelope functions (see equation (2)). On the left side, the pulse is perfectly symmetric ($T_1 = T_2 = 500$ fs), while the right side corresponds to a completely asymmetric ($T_1 = 1000$ fs; $T_2 = 0$) laser pulses. The pulse area is kept constant by imposing the condition $T_1 + T_2 = 2T$, with $T = 500$ fs. The applied photon energy is the same as in figure 7, $\omega = 4.18$ eV. The presented results were obtained from wave packet propagations.

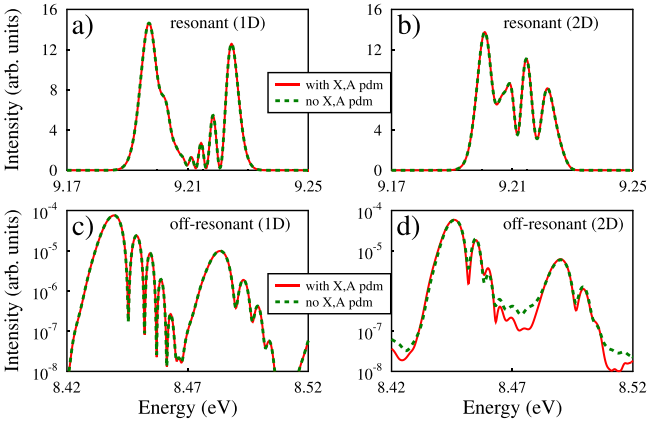

Figure 10. Energy spectra of MgH^+ obtained from wave packet propagations, either including (solid lines) or omitting (dashed lines) the permanent dipole moments of the X and A electronic states. For resonant driving in (a),(b), the laser parameter values are identical to those in figure 5. In the case of off-resonant driving in (c),(d), the laser parameter values agree with those in figure 7. The 1D results were obtained with equation (5), while the 2D spectra were obtained with equation (10) of the appendix, initializing the rotating-vibrating molecule in the state $X(\nu = 0, J = 1)$.

2.4. Rotating-vibrating MgH^+

To provide a more accurate description of the above-discussed phenomena, and to reveal some peculiarities of molecular resonance dissociation versus atomic resonance ionization, below we solve the 2D TDSE of MgH^+ under various conditions. As seen in figure 10(b), when the resonantly driven molecule is allowed to dynamically rotate, the spectrum contains four peaks instead of five, indicating that the number of completed Rabi floppings is reduced from five to four (not shown here). This is a direct consequence of the reduced effective intensity felt by the rotating-vibrating molecule, which is not aligned perfectly with the laser polarization, unlike in the 1D case. Owing to the additional θ degree of freedom (DOF), several closely-spaced rotational states are available for the molecule

in the 2D case. As these states lie within the pulse bandwidth, the population is distributed among them. This leads to a decreased contrast of the Rabi floppings which is also reflected in the decreased contrast of the spectral peaks in figure 10(b). Another consequence of the reduced effective intensity in 2D is the smaller splitting of the spectrum. When the molecule is driven off-resonantly, the number and contrast of the spectral peaks are also reduced in the 2D case (see figures 10(c) and (d)). These masking effects found for rotating-vibrating molecules are somewhat disadvantageous as compared to atomic REMPI, but the main spectral features still remain observable.

As seen in figure 10, the electric permanent dipoles of the bound states X and A do not have a substantial impact on the spectrum shape. In contrast, however, the permanent dipole of the dissociative C state strongly modifies the spectrum shape in the off-resonant case, as it was shown before in figures 8(b) and (c). In fact, the pdm of the C state prevents the observation of the effect of DI, revealed by asymmetric pulses in figure 8(b). It is another drawback compared to the REMPI of atoms that have no permanent dipoles. Therefore, studying the impact of DI in molecules is expected to be more advantageous with molecules that have no permanent dipole.

Finally, we notice that observing the spectral features presented here for molecules typically requires higher resolution as compared to resolving photoelectron signatures in atomic REMPI. This is a natural consequence of the much smaller energetic separation of vibrational or rovibrational levels, compared to that of the electronic states in atoms.

3. Summary

We have studied the resonance-enhanced two-photon dissociation of the MgH^+ molecular ion, mediated by different vibrational levels of an intermediate bound electronic state potential. On the basis of wave packet propagations, that were supported by a multi-level model, we found that, when the laser frequency is tuned to exact resonance with one of these vibrational levels, Rabi oscillations are efficiently generated. The interference of molecular fragment amplitudes that are emitted at each Rabi cycle, leads to pronounced multipeak patterns in the spectrum of the dissociating molecule.

On the other hand, when the laser is tuned out of resonance, Rabi oscillations are washed out and the multipeak spectral pattern is mainly caused by the DI of fragment amplitudes, that were emitted with the same energy but with a time delay, at the rising- and falling edges of the laser pulse. Thus, the photon frequency was found a key parameter in the competition of these two dynamical effects, Rabi oscillations and DI, in agreement with similar findings reported on atomic ionization [56, 57]. For an experimental observation of the general phenomena discussed in this paper, the applied laser pulse parameter ranges are routinely available in laboratories. However, observing the low kinetic energy molecular fragments with high precision ($\sim$1 meV)—that is beyond the resolution of vibrational level spacings—can be challenging with present capabilities [64]. This is a drawback compared to the observation of the energy distribution of photoelectrons in REMPI, which typically requires lower resolution [37].

Fine tuning the photon wavelength also allowed for an efficient control of the dissociation yield and of the bound-state dynamics. This efficient control was made possible by the sensitive energy-dependence of the dipole coupling strength of the bound levels with the continuum (figure 3), which is expected to be a general feature of molecular systems.

Finally, we have shown that the application of laser pulse envelopes with different asymmetric temporal profiles can also allow one to efficiently control the dissociation yield. A gradual shut-down of the falling edge of the off-resonant laser pulse can strongly enhance the dissociation probability by prohibiting recapture from the continuum.

Data availability statement

The data cannot be made publicly available upon publication because no suitable repository exists for hosting data in this field of study. The data that support the findings of this study are available upon reasonable request from the authors.

Acknowledgments

A C is grateful for the support of the János Bolyai Research Scholarship (BO/00474/22/11) of the Hungarian Academy of Sciences. A Tóth is acknowledged for valuable discussions. The authors are indebted to NKFIH for funding (Grant No. K146096). Supported by the University of Debrecen Program for Scientific Publication.

Author contributions

Dilfuza Umarova 0009-0008-4009-110X
Software (equal), Writing – original draft (equal)

Otabek Umarov 0000-0002-9987-5629
Software (equal), Writing – original draft (equal)

András Csehi 0000-0002-8794-6610
Conceptualization (lead), Writing – original draft (equal)

Appendix. Methods

In this appendix, we provide the details of the numerical methods utilized in this paper to study the $(1+1)$ photon resonance-enhanced photodissociation of the MgH^+ molecular ion (figure 1). Working in the Born–Oppenheimer picture, we solve the time-dependent Schrödinger equation of the nuclei accurately, and with an approximate method that is able to capture the spectral characteristics of the dissociating molecule. This model can help elucidating the system dynamics and the structural buildup of the fragment energy spectra. For the sake of clarity, in the majority of the paper, we consider vibrating molecules that are parallel with the laser polarization direction (the z direction). Extension of this description to rotating-vibrating molecules is also presented.

Throughout this work, linearly polarized laser pulses are applied, given by the general expression (atomic units are used unless stated otherwise)

$$\varepsilon(t) = \varepsilon_0 g(t)\cos(\omega t). \tag{3}$$

Here, ε_0 is the electric field amplitude, ω is the carrier angular frequency, and $g(t)$ is the envelope function. In the majority of the paper, symmetric Gaussian envelope functions are considered

$$g(t) = \mathrm{e}^{-t^2/T^2}, \tag{4}$$

with T being the pulse duration parameter that is related to the full width at half maximum as fwhm $= T\sqrt{2\ln 2}$. In section 2.3, Gaussian envelopes with an asymmetric temporal profile are also utilized.

A.1. Wave packet propagation (1D)

For an accurate description of the photodissociation dynamics of vibrating MgH^+, the time-dependent Schrödinger equation of the nuclei was propagated. Within the space of the three relevant electronic states, the vibrational dynamics is governed by the 3×3 Hamiltonian in the dipole approximation

$$H(t) = \left(-\frac{1}{2M_\mathrm{r}}\frac{\partial^2}{\partial R^2}\right)\mathbf{1} + \begin{pmatrix} U_X & 0 & 0 \\ 0 & U_A & 0 \\ 0 & 0 & U_C \end{pmatrix} - \varepsilon(t)\begin{pmatrix} d_X & d_{XA} & d_{XC} \\ d_{AX} & d_A & d_{AC} \\ d_{CX} & d_{CA} & d_C \end{pmatrix}. \tag{5}$$

Here, M_r is the reduced mass, R is the internuclear coordinate, and $\mathbf{1}$ denotes the 3×3 unit matrix. $U_n(R)$ are the potential energy curves of the involved electronic states (see figure 1), $d_n(R)$ are the electric permanent dipoles, and $d_{mn}(R)$ are the electric transition dipoles $(m,n = X,A,C)$. These *ab initio* data were taken from [59] (for the dipole curves, see figure 11).

The TDSE characterized by the Hamiltonian in equation (5), was solved with the multi-configurational time-dependent Hartree (MCTDH) method [65, 66]. The R radial DOF was defined on an fft-DVR (discrete variable representation) grid with N_R primitive basis elements distributed in the range $1.5\,\mathrm{au} \leqslant R \leqslant 40\,\mathrm{au}$. In the MCTDH wave function representation, these primitive basis functions (ξ) build up the ϕ single particle functions, the time-dependent linear combinations of which form the Ψ total wave function

$$\phi_{j_R}^{(R)}(R,t) = \sum_{i=1}^{N_R} c_{j_R i}^{(R)}(t)\,\xi_i^{(R)}(R)$$
$$\Psi(R,t) = \sum_{j_R=1}^{n_R} A_{j_R}(t)\,\phi_{j_R}^{(R)}(R,t). \tag{6}$$

For a proper convergence of the numerical propagations, $N_R = 4096$ basis functions have been used, with $n_R = 10$ for each electronic state. The time-propagation was performed with the variable mean-field integration scheme of the MCTDH framework. The equations of motion were propagated with the Adams–Bashforth–Moulton predictor-corrector method with properly chosen parameter values for the integration order (6), error tolerance (10^{-7}) and step size $(10^{-4}\,\mathrm{fs})$. To minimize reflections and transmissions, caused by the finite size of the radial box (the radial grid size was $R_\mathrm{max} = 40\,\mathrm{au}$), CAP has been utilized at the last 10 au of the radial grid (starting at $R_\mathrm{c} = 30\,\mathrm{au}$)

$$-\mathrm{i}W(R) = -\mathrm{i}\zeta|R - R_\mathrm{c}|^b\Theta(R - R_\mathrm{c}). \tag{7}$$

Here, the parameter values $\zeta = 6.67\times 10^{-5}$, $b = 3$ were optimized, and $\Theta(x)$ is the Heaviside step function. With the help of the propagated nuclear wave packets, the electronic state populations were calculated as

$$p_n(t) = \langle\Psi_n(R,t)\,|\,\Psi_n(R,t)\rangle \quad (n = X,A,C), \tag{8}$$

while the p_diss dissociation probability in the C electronic state was obtained as part of $p_C(t)$ that was absorbed by the CAP.

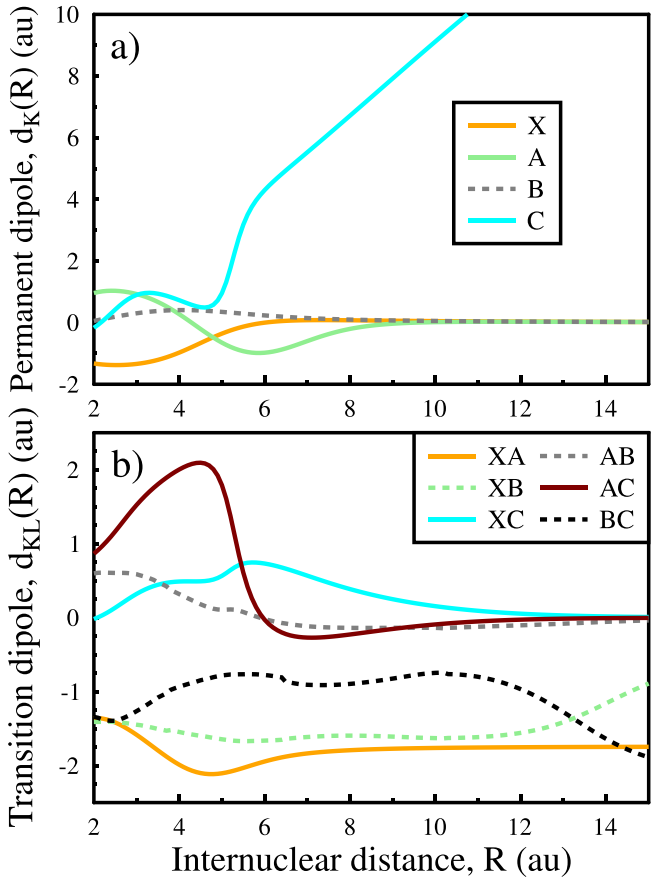

Figure 11. Electric permanent (a) and transition (b) dipole moments of the MgH^+ molecule, applied in the full calculations.

Finally, the energy spectrum of the dissociating photofragments with energy ω_ε, was calculated using the CAP as

$$\sigma(\omega_\varepsilon) = \int_0^\infty \mathrm{d}t \int_0^\infty \mathrm{d}t' \langle \Psi(t)|W|\Psi(t')\rangle \mathrm{e}^{-\mathrm{i}\omega_\varepsilon(t-t')}. \quad (9)$$

A.2. Wave packet propagation (2D)

In the most general case, the total Hamiltonian of rotating-vibrating MgH^+, in the space of the four relevant electronic states, has the following form

$$H(t) = \left(-\frac{1}{2M_r}\frac{\partial^2}{\partial R^2} + \frac{\mathcal{J}^2}{2M_r R^2}\right)\mathbf{1} + \begin{pmatrix} U_X & 0 & 0 & 0 \\ 0 & U_A & 0 & 0 \\ 0 & 0 & U_B & 0 \\ 0 & 0 & 0 & U_C \end{pmatrix} - \varepsilon(t)\begin{pmatrix} d_X\cos\theta & d_{XA}\cos\theta & d_{XB}\sin\theta & d_{XC}\cos\theta \\ d_{AX}\cos\theta & d_A\cos\theta & d_{AB}\sin\theta & d_{AC}\cos\theta \\ d_{BX}\sin\theta & d_{BA}\sin\theta & d_B\cos\theta & d_{BC}\sin\theta \\ d_{CX}\cos\theta & d_{CA}\cos\theta & d_{CB}\sin\theta & d_C\cos\theta \end{pmatrix}, \quad (10)$$

where M_r is the reduced mass, R is the internuclear coordinate and θ is the angle of rotation measured between the laser polarization and the axis of the molecule. $\mathcal{J}$ is the angular momentum operator, while $\mathbf{1}$ denotes the 4×4 unit matrix. $U_n(R)$ are the potential energy curves of the considered electronic states, while $d_n(R)$ are the electric permanent dipoles and $d_{mn}(R)$ are the electric transition dipoles $(m,n = X,A,B,C)$ (see figure 11). We note here that the B state is not expected to play a significant role as it is perpendicular to the other states plus it is off-resonant, but for the sake of completeness we included it in the 2D description.

The MCTDH wave function representation in the case of rotating-vibrating molecule is a generalization of equation (6)

$$\phi_{j_q}^{(q)}(q,t) = \sum_{i=1}^{N_q} c_{j_q i}^{(q)}(t)\,\xi_i^{(q)}(q) \qquad (q = R,\theta)$$
$$\Psi(R,\theta,t) = \sum_{j_R=1}^{n_R}\sum_{j_\theta=1}^{n_\theta} A_{j_R,j_\theta}(t)\,\phi_{j_R}^{(R)}(R,t)\,\phi_{j_\theta}^{(\theta)}(\theta,t). \quad (11)$$

The additional rotational DOF θ was described by N_θ Legendre polynomials, $P_J^m(\cos\theta)$ with $m=0$ and $J = 0,1,\ldots,N_\theta-1$. To ensure proper convergence, $N_R = 4096$ and $N_\theta = 91$ basis functions have been utilized. Furthermore, the number of SPFs were ranging between $n_R = n_\theta = 5-10$ for both DOFs, on each electronic state.

A.3. Multi-level model

To gain insight into the role of the individual vibrational levels in the formation of the spectrum, we introduce a simplified, yet instructive description of the nuclear dynamics. In this model, the total time-dependent wave function of the molecule is expanded in the basis of the $|k\rangle$ eigenstates of the H_0 Hamiltonian of the free molecule, dressed by the respective ω_k eigenenergies

$$\Psi(t) = \sum\!\!\!\!\!\!\int_k c_k(t)\,|k\rangle \mathrm{e}^{-\mathrm{i}\omega_k t}. \quad (12)$$

Upon inserting equation (12) into the TDSE $\mathrm{i}\dot{\Psi} = [H_0 + V(t)]\Psi$, one obtains the set of coupled differential equations for the bound and continuum population amplitudes

$$\mathrm{i}\dot{c}_j(t) = \sum\!\!\!\!\!\!\int_k c_k(t)\,\mathrm{e}^{-\mathrm{i}\omega_{kj}t} V_{jk}(t). \quad (13)$$

In equation (13), the energy differences $\omega_{kj} = \omega_k - \omega_j$ have been introduced, and the dipole interaction matrix elements are written as $V_{jk}(t) = -\varepsilon(t)\mu_{jk}$. Here, the nuclear dipole elements $\mu_{jk} = \langle j|d(R)|k\rangle$ between states $|j\rangle$ and $|k\rangle$ are calculated with the $d(R)$ electric transition- or permanent dipole moments. Including all the bound and continuum states of MgH^+ in equation (13), would allow for the exact solution of the vibrational dynamics. However, for practical reasons, here we have restricted the infinite state space to the physically relevant levels, including the 17 and 15 lowest states in the X and A electronic states, respectively. Furthermore, 400 continuum states within the actual, relevant energy region of the C manifold have been considered, to calculate the spectrum accurately. Utilizing the propagated population amplitudes, the vibrational state populations have been obtained as $p_k(t) = |c_k(t)|^2$, while the spectrum was calculated as $\sigma(\omega_\varepsilon) = |c_\varepsilon(t\to\infty)|^2$, after the pulse has expired.

The solution of equation (13) was carried out with the fourth order Runge–Kutta method. Since we focus on the first photopeak here, the continuum–continuum dipoles ($\mu_{\varepsilon\varepsilon'}$) have been omitted. Furthermore, the permanent dipole terms μ_{kk} could be also omitted, as they were found to have negligible impact on the populations and on the spectra. Such permanent dipole terms become important e.g. in low-frequency infrared laser fields [67]. As will be clear from the discussion in section 2, the populations and spectra provided by the multi-level model are nicely supported by the those obtained from accurate wave packet propagations.

References

[1] Shapiro M and Brumer P 2003 *Principles of the Quantum Control of Molecular Processes* (Wiley)

[2] Warren W S, Rabitz H and Dahleh M 1993 Coherent control of quantum dynamics: the dream is alive *Science* **259** 1581

[3] Rabitz H, de Vivie-Riedle R, Motzkus M and Kompa K 2000 Whither the future of controlling quantum phenomena? *Science* **288** 824

[4] Wollenhaupt M, Engel V and Baumert T 2005 Femtosecond laser photoelectron spectroscopy on atoms and small molecules: prototype studies in quantum control *Annu. Rev. Phys. Chem.* **56** 25

[5] Tannor D J 1994 *Molecules in Laser Fields* ed A D Bandrauk (Marcel Dekker)

[6] Rice S A and Zhao M 2000 *Optical Control of Molecular Dynamics* (*Baker Lecture Series*) (Wiley)

[7] Bergmann K, Theuer H and Shore B W 1998 Coherent population transfer among quantum states of atoms and molecules *Rev. Mod. Phys.* **70** 1003

[8] Tannor D J and Rice S A 1988 Coherent pulse sequence control of product formation in chemical reactions *Adv. Chem. Phys.* **70** 441

[9] Vitanov N V, Halfmann T, Shore B W and Bergmann K 2001 Laser-induced population transfer by adiabatic passage techniques *Annu. Rev. Phys. Chem.* **52** 763

[10] Solá I R, Chang B Y and Rabitz H 2003 Manipulating bond lengths adiabatically with light *J. Chem. Phys.* **119** 10653

[11] Sussman B J, Townsend D, Ivanov M and Stolow A 2006 Dynamic stark control of photochemical processes *Science* **314** 278

[12] Trallero-Herrero C, Cohen J L and Weinacht T C 2006 Strong-field atomic phase matching *Phys. Rev. Lett.* **96** 063603

[13] Sala M, Saab M, Lasorne B, Gatti F and Guérin S 2014 Laser control of the radiationless decay in pyrazine using the dynamic Stark effect *J. Chem. Phys.* **140** 194309

[14] Solá I R, Chang B Y, Malinovskaya S A and Malinovsky V S 2018 Quantum control in multilevel systems *Adv. At. Mol. Opt. Phys.* **67** 151

[15] Fábri C, Marquardt R, Császár A G and Quack M 2019 Controlling tunneling in ammonia isotopomers *J. Chem. Phys.* **150** 014102

[16] Csehi A 2019 Control of the populations and phases of two-level quantum systems by a single frequency-chirped laser pulse *J. Phys. B: At. Mol. Opt. Phys.* **52** 195004

[17] Fagundes F S and de Lima E F 2024 Reverse engineering control of the relative phase and populations of two-level quantum systems *Phys. Rev. A* **110** 022201

[18] Elarabi A A and Csehi A 2025 Exactly solvable two-level model with time-dependent coupling, detuning and loss: application to strong-field resonance ionization *Phys. Rev. A* **111** 063108

[19] Banerjee S, Chakrabarti M K, Bhattacharyya S S and Saha S 1991 Resonance enhanced two-photon dissociation of H_2 by the X - (EF+GK+I) transition via intermediate B,C states *J. Chem. Phys.* **95** 1608

[20] Datta A, Saha S and Bhattacharyya S S 1999 Resonance-enhanced two-photon dissociation of H_2 through nonadiabatically coupled intermediate and final states *Phys. Rev. A* **60** 1324

[21] Liu K, Li Q, Lan P and Lu P 2015 Enhanced dissociation of H_2^+ into highly excited states by UV pulses *Mol. Phys.* **113** 3247

[22] García-Vela A and Bañares L 2013 Wave packet study of the methyl iodide photodissociation dynamics in the 266-333 nm wavelength range *Eur. Phys. J. D* **67** 265

[23] Casasús I M, Corralesa M E and Bañares L 2022 Wavelength dependence of the multiphoton ionization of CH3I by intense femtosecond laser pulses through Freeman resonances *Phys. Chem. Chem. Phys.* **24** 29616

[24] Bunjac A, Popović D B and Simonović N S 2017 Resonant dynamic Stark shift as a tool in strong-field quantum control: calculation and application for selective multiphoton ionization of sodium *Phys. Chem. Chem. Phys.* **19** 19829

[25] Delone N B and Krainov V P 1999 AC Stark shift of atomic energy levels *Phys.-Usp.* **42** 669

[26] Sussman B J 2011 Five ways to the nonresonant dynamic Stark effect *Am. J. Phys.* **79** 477

[27] Rabi I I 1937 Space quantization in a gyrating magnetic field *Phys. Rev.* **51** 652

[28] Autler S H and Townes C H 1955 Stark effect in rapidly varying fields *Phys. Rev.* **100** 703

[29] Bayer T, Wollenhaupt M, Braun H and Baumert T 2016 Ultrafast and efficient control of coherent electron dynamics via SPODS *Adv. Chem. Phys.* **159** 235

[30] Bayer T, Eickhoff K, Köhnke D and Wollenhaupt M 2023 Phase control of the Autler-Townes doublet in multistate systems *Phys. Rev. A* **108** 033111

[31] Tóth A and Csehi A 2021 Probing strong-field two-photon transitions through dynamic interference *J. Phys. B: At. Mol. Opt. Phys.* **54** 035005

[32] Tóth A, Borbély S, Zhou Y and Csehi A 2023 Role of dynamic Stark shifts in strong-field excitation and subsequent ionization *Phys. Rev. A* **107** 053101

[33] Tóth B, Tóth A and Csehi A 2024 Competition of multiphoton ionization pathways in lithium *J. Phys. B: At. Mol. Opt. Phys.* **57** 055002

[34] Bunjac A, Popović D B and Simonović N S 2022 Analysis of the asymmetry of Autler-Townes doublets in the energy spectra of photoelectrons produced at two-photon ionization of atoms by strong laser pulses *Eur. Phys. J. D* **76** 249

[35] Olofsson E and Dahlström J M 2023 Photoelectron signature of dressed-atom stabilization in an intense XUV field *Phys. Rev. Res.* **5** 043017

[36] Zhang X, Zhou Y, Liao Y, Chen Y, Liang J, Ke Q, Li M, Csehi A and Lu P 2022 Effect of nonresonant states in near-resonant two-photon ionization of hydrogen *Phys. Rev. A* **106** 063114

[37] Nandi S *et al* 2022 Observation of Rabi dynamics with a short-wavelength free-electron laser *Nature* **608** 488

[38] Richter F *et al* 2024 Strong-field quantum control in the extreme ultraviolet domain using pulse shaping *Nature* **636** 337

[39] Zhang X, Liao Y, Chen Y, Yu M, Liu K, Lu P and Zhou Y 2024 Characterization of the two-photon transition phase in the buildup process of Rabi oscillations *Phys. Rev. A* **109** 033101

[40] Deng Y, Zhang X, Zhou Y and Lu P 2025 Time- and energy-domain interference in the dynamically dressed Rabi-cycling atom *Phys. Rev. A* **111** 043110

[41] Wan W-q, Liu G-Y, Xie M-F, Meng Q-B and Jiang W-C 2025 Temporal interference picture for subpeak structures between Autler-Townes doublets in photoelectron energy spectra *Phys. Rev. A* **111** 033117

[42] Guangyin L, Weichao J and Liangyou P 2024 Photoionization of atoms and molecules by strong XUV pulses *Acta Opt. Sin.* **44** 1732001

[43] Li W, Wang Y, Li X, Yang T, Zhang D and Ding D 2025 Direct observation of two-photon-resonance Autler-Townes splitting of atomic sodium *Phys. Rev. A* **111** 063102

[44] Demekhin P V and Cederbaum L S 2012 Dynamic interference of photoelectrons produced by high-frequency laser pulses *Phys. Rev. Lett.* **108** 253001

[45] Baghery M, Saalmann U and Rost J M 2017 Essential conditions for dynamic interference *Phys. Rev. Lett.* **118** 143202

[46] Jiang W-C and Burgdörfer J 2018 Dynamic interference as signature of atomic stabilization *Opt. Express* **26** 19921

[47] Toyota K, Tolstikhin O I, Morishita T and Watanabe S 2007 Siegert-state expansion in the Kramers-Henneberger frame: interference substructure of above-threshold ionization peaks in the stabilization regime *Phys. Rev. A* **76** 043418

[48] Tolstikhin O I 2008 Siegert-state expansion for nonstationary systems. IV. Three-dimensional case *Phys. Rev. A* **77** 032712

[49] Demekhin P V and Cederbaum L S 2013 AC Stark effect in the electronic continuum and its impact on the photoionization of atoms by coherent intense short high-frequency laser pulses *Phys. Rev. A* **88** 043414

[50] Wang M-X, Liang H, Xiao X-R, Chen S-G, Jiang W-C and Peng L-Y 2018 Nondipole effects in atomic dynamic interference *Phys. Rev. A* **98** 023412
[51] Liang H, Jiang W-C, Wang M-X, Gong Q, Krajewska K and Peng L-Y 2020 Dynamical interference of H and H_2^+ in one-photon ionization *Phys. Rev. A* **101** 053424
[52] Wang M-X, Chen S-G, Liang H and Peng L-Y 2020 Review on non-dipole effects in ionization and harmonic generation of atoms and molecules *Chin. Phys. B* **29** 013302
[53] Wang J, Li G-L, Liu X, Zhu F-Z, Jiao L-G and Liu A 2022 Photoelectron momentum distribution of hydrogen atoms in a superintense ultrashort high-frequency pulse *Front. Phys.* **10** 974500
[54] Jiang W-C, Chen S-G, Peng L-Y and Burgdörfer J 2020 Two-electron interference in strong-field ionization of he by a short intense extreme ultraviolet laser pulse *Phys. Rev. Lett.* **124** 043203
[55] Li M *et al* 2024 Observation of laser-assisted dynamic interference by attosecond controlled photoelectron spectroscopy *Phys. Rev. Lett.* **133** 253201
[56] Tóth A, Borbély S and Csehi A 2023 Dynamic interference in below-threshold ionization *Phys. Rev. A* **108** L061101
[57] Elarabi A A and Csehi A 2025 Transition from Rabi oscillations to dynamic interference: the multipeak pattern of the Autler-Townes doublet revisited *Phys. Rev. A* **111** 033107
[58] Kahra S *et al* 2012 A molecular conveyor belt by controlled delivery of single molecules into ultrashort laser pulses *Nat. Phys.* **8** 238
[59] Badankó P, Halász G J, Cederbaum L S, Vibók A and Csehi A 2018 Substantial impact of the orientation of transition dipole moments on the dynamics of diatomics in laser fields *J. Chem. Phys.* **149** 181101
[60] Liu Y R, Wu Y, Wang J G, Vendrell O, Kimberg V and Zhang S B 2020 Electron-rotation coupling in diatomics under strong-field excitation *Phys. Rev. A* **102** 033114
[61] Liu Y R, Kimberg V, Wu Y, Wang J G, Vendrell O and Zhang S B 2022 Electron-rotation coupling in UV photodissociation of aligned diatomics *Phys. Rev. Res.* **4** 013066
[62] Umarova D, Umarov O, Tóth A and Csehi A 2024 Spectral evidence of vibronic Rabi oscillations in the resonance-enhanced photodissociation of MgH^+ *Phys. Rev. A* **110** 033112
[63] Ning Q-C, Saalmann U and Rost J M 2018 Electron dynamics driven by light-pulse derivatives *Phys. Rev. Lett.* **120** 033203
[64] Suits A G 2018 Invited review article: photofragment imaging *Rev. Sci. Instrum.* **89** 111101
[65] Beck M H, Jäckle A, Worth G A and Meyer H-D 2000 The multiconfiguration time-dependent Hartree (MCTDH) method: a highly efficient algorithm for propagating wavepackets *Phys. Rep.* **324** 1
[66] Meyer H-D, Gatti F and Worth G A 2009 *Multidimensional Quantum Dynamics: Mctdh Theory and Applications* (Wiley-VCH)
[67] Varró S, Hack S, Paragi G, Földi P, Barna I F and Czirják A 2023 Diatomic molecule in a strong infrared laser field: level-shifts and bond-length change due to laser-dressed Morse potential *New J. Phys.* **25** 073001